NANO · MICRO small
www.small-journal.com

Lewis Acid Site Assisted Bifunctional Activity of Tin Doped Gallium Oxide and Its Application in Rechargeable Zn-Air Batteries

Aruna Narayanan Nair, Mohamed F. Sanad, Rahul Jayan, Guillermo Gutierrez, Yulu Ge, Md Mahbubul Islam, Jose A. Hernandez-Viezcas, Vishal Zade, Shalini Tripathi, Vaithiyalingam Shutthanandan, Chintalapalle V. Ramana, and Sreeprasad T. Sreenivasan**

The enhanced safety, superior energy, and power density of rechargeable metal-air batteries make them ideal energy storage systems for application in energy grids and electric vehicles. However, the absence of a cost-effective and stable bifunctional catalyst that can replace expensive platinum (Pt)-based catalyst to promote oxygen reduction reaction (ORR) and oxygen evolution reaction (OER) at the air cathode hinders their broader adaptation. Here, it is demonstrated that Tin (Sn) doped β-gallium oxide (β-Ga_2O_3) in the bulk form can efficiently catalyze ORR and OER and, hence, be applied as the cathode in Zn-air batteries. The Sn-doped β-Ga_2O_3 sample with 15% Sn ($Sn_{x=0.15}$-Ga_2O_3) displayed exceptional catalytic activity for a bulk, non-noble metal-based catalyst. When used as a cathode, the excellent electrocatalytic bifunctional activity of $Sn_{x=0.15}$-Ga_2O_3 leads to a prototype Zn-air battery with a high-power density of 138 mW cm^{-2} and improved cycling stability compared to devices with benchmark Pt-based cathode. The combined experimental and theoretical exploration revealed that the Lewis acid sites in β-Ga_2O_3 aid in regulating the electron density distribution on the Sn-doped sites, optimize the adsorption energies of reaction intermediates, and facilitate the formation of critical reaction intermediate (O*), leading to enhanced electrocatalytic activity.

1. Introduction

Metal-air batteries, which generate electricity through a redox reaction between metal and oxygen, are promising candidates as future power sources due to their remarkably high theoretical energy output.[1–4] For instance, Zinc-air batteries are predicted to have a high theoretical specific energy density of 1086 W h kg^{-1}, which is 2.5 times higher than state-of-the-art lithium-ion batteries.[5–8] The key to the functioning of Zn-air batteries is two electrochemical reactions occurring at the air cathode, namely oxygen reduction reaction (ORR) during discharging and oxygen evolution reaction (OER) during charging. Consequently, the inferior performance of the air cathode leads to the Zinc-air batteries displaying lower energy output than the theoretical value. Hence, catalysts with excellent catalytic efficacy towards ORR (e.g., Pt) and OER (e.g., RuO_2) are employed in the air cathode to enhance the performance of Zn-air batteries. However, the poor stability, high cost, and scarcity of state-of-the-art catalysts such as Pt or RuO_2 make the technology commercially untenable. Thus, the widespread adoption of Zinc-air batteries depends on discovering low-cost, highly active, stable, and potentially bifunctional electrocatalysts. Recently, transition metal oxide (TMO) systems emerged as viable ORR and OER electrocatalysts due to their competent

A. N. Nair, M. F. Sanad, Y. Ge, J. A. Hernandez-Viezcas, S. T. Sreenivasan
Department of Chemistry and Biochemistry
The University of Texas at El Paso
El Paso, TX 79968, USA
E-mail: sreenivasan@utep.edu

M. F. Sanad
Department of Environmental Sciences and Engineering
The University of Texas at El Paso
El Paso, TX 79968, USA

R. Jayan, M. M. Islam
Department of Mechanical Engineering
Wayne State University
Detroit, MI 48202, USA

G. Gutierrez, V. Zade, C. V. Ramana
Center for Advanced Materials Research (CMR)
The University of Texas at El Paso
El Paso, TX 79968, USA
E-mail: rvchintalapalle@utep.edu

S. Tripathi
Energy and Environment Directorate
Pacific Northwest National Laboratory
Richland, WA 99352, USA

V. Shutthanandan
Environmental Molecular Sciences Laboratory (EMSL)
Pacific Northwest National Laboratory (PNNL)
Richland, WA 99352, USA

The ORCID identification number(s) for the author(s) of this article can be found under https://doi.org/10.1002/smll.202202648.

DOI: 10.1002/smll.202202648

activity and better stability.[9–14] A variety of non-precious metal oxide catalysts (Co_3O_4, FeO_x, and MnO_x, etc.), especially in the nanoform, demonstrated high catalytic activity.[15–19] Nonetheless, most nano-TMO catalysts suffer from poor conductivity and agglomeration-induced loss of active sites, leading to inferior or gradually degrading catalytic activity.

Tailoring fundamental material properties such as acidity/basicity, work function, and density of states near the Fermi level can affect the charge distribution on the active sites of catalysts. Recent research revealed that Lewis acid sites adjacent to the catalytic sites could influence their activity for oxygen redox reactions.[20] Theoretical studies indicated that in Lewis acid catalysts, the metal atoms could coordinate with an adjacent electronegative atom with a lone pair, resulting in a charge transfer between them.[] Gallium oxide (Ga_2O_3) in its most stable form, β-Ga_2O_3 with tetrahedral and octahedral Ga ions (Ga^{3+}), is a strong Lewis acid where tetrahedral Ga^{3+} is the Lewis acid center.[22] Recently, β-Ga_2O_3-based photocatalysts gained increased attention due to their significant potential for activating CO_2. They have also been recognized as alkane dehydrogenation catalysts because of their unique ability to activate hydrocarbons.[23,24] However, despite their wide use in catalysis, the exploration of β-Ga_2O_3 as an electrocatalyst remains underexplored. Recently, Kakoria et al. investigated the electrocatalytic activity of electrospun β-Ga_2O_3 nanofibers towards hydrogen evolution reaction (HER) and ORR.[25] Nevertheless, like other nanosystems, nanofiber catalysts are prone to aggregation and hence have inferior long-term stability. Liu et al investigated the role of oxygen vacancies in OER catalyzed by β-Ga_2O_3 using density functional theory (DFT).[26] But, experimental investigation of such systems is still unexplored in detail. Alternately, engineering the electron distribution and Lewis acidity of β-Ga_2O_3 could be the key to realizing inexpensive, high-performance, multifunctional, and stable catalysts without morphological and dimensional modifications. Recent research proved that lattice incorporation of appropriate dopants could modulate the electronic distribution, band structure, and catalytic activity of materials.[27–33] For example, Tin (Sn) doping improves the sluggish kinetics of OER/ORR because the oxygen-bound intermediates can interact favorably on the Sn surface.[22,34–38]

Anticipating synergistic effects due to the Lewis acid sites in β-Ga_2O_3 and the favorable oxygen adsorption properties of Sn, we atomically doped β-Ga_2O_3 with Sn to derive excellent bulk bifunctional electrocatalyst towards ORR and OER, for the first time. Here, the β-Ga_2O_3 was synthesized via the high-temperature, solid-state route and doped with different Sn percentages (x = 0.05–0.20).[39] Interestingly, a superior bifunctional ORR and OER activity, the best activity reported for a bulk sample, was demonstrated at 15% doping of Sn (x = 0.15, denoted as $Sn_{x=0.15}$-Ga_2O_3) with a lower overpotential and higher current density. Our experimental investigations revealed that the lattice incorporation of Sn leads to modification of the bandgap, decreases the charge-transfer resistance, and introduces new highly catalytic centers in the β-Ga_2O_3 lattice. Our theoretical exploration indicated that the addition of Sn near the Lewis acid coordination sites triggers an electron transfer from the Ga^{3+} to the adjacent Sn–O bond leading to a redistribution of the electron density and a significant decrease in activation energy on the surface of Sn-doped β-Ga_2O_3, accounting for the enhanced catalytic performance. Bader charge analysis of the intermediate steps proved the importance of the Ga^{3+} Lewis acid sites in augmenting the catalytic activity of doped Sn sites. Finally, we leveraged $Sn_{x=0.15}$-Ga_2O_3 as the air cathode of a Zn-air battery, which demonstrated significantly improved stability and reduced polarizability compared to devices with benchmark Pt and RuO_2 electrocatalysts, pointing to the potential of $Sn_{x=0.15}$-Ga_2O_3 for electrochemical energy storage applications.

2. Results and Discussion

2.1. Structure and Chemistry

Among the different crystal forms of Ga_2O_3, β-Ga_2O_3 is the most stable (melting point 1740 °C), with the oxide ions in distorted ccp arrangement and Ga^{3+} occupying distorted tetrahedral and octahedral sites. Further, β-Ga_2O_3 is stabilized in monoclinic crystal symmetry with the C2/m space group at ambient conditions.[39–41] The prepared β-Ga_2O_3 and Sn_x-Ga_2O_3 samples were analyzed using different microscopic and spectroscopic techniques to confirm the Sn doping and derive an in-depth understanding of their morphology, structure, and surface chemistry. We recently reported a detailed account of crystallography, Rietveld refinement, structure, and surface morphology of the Sn-doped Ga_2O_3.[39] **Figure 1**a shows the XRD patterns of pristine β-Ga_2O_3 and $Sn_{x=0.15}$-Ga_2O_3.[42] While lower levels of doping lead to lattice incorporation, increasing the concentration of Sn (e.g., $Sn_{x=0.2}$-Ga_2O_3) resulted in the formation of a secondary SnO_2 phase, as evidenced by the XRD.[39] Figure 1b shows the Raman spectra of β-Ga_2O_3 and $Sn_{x=0.15}$-Ga_2O_3 samples using a 532 nm laser excitation. The corresponding Raman spectrum of other Sn dopant ratios is given in Figure S1, Supporting Information. The features in the Raman spectrum can be divided into three groups, namely low-frequency mode (below 200 cm^{-1}), mid-frequency mode (500–300 cm^{-1}), and high-frequency mode (770–500 cm^{-1}), all of which are related to different vibrational modes of Ga_2O_3.[43] All relevant Raman vibration modes of Ga_2O_3 are visible in parent β-Ga_2O_3 and Sn-doped Ga_2O_3 samples (Figure 1b). The Raman bands at 140, 166, and 195 cm^{-1} are due to vibration of Ga–O chains; 345, 414, and 475 cm^{-1} belong to the deformation of $GaI(OI)_2$ octahedra; 652 and 767 cm^{-1} are because of the symmetric stretching of GaO_4 tetrahedra.[44] Figure S2, Supporting Information shows the Raman bands of the SnO_2 at 482, 633, and 775 cm^{-1}, which corresponds to the E_g, A_{1g}, and B_{2g} vibrational modes, respectively.[45] The close overlap of features from β-Ga_2O_3 and SnO_2 made it challenging to confirm the Sn doping using Raman spectroscopy. However, the presence of relevant features of β-Ga_2O_3 in the undoped and doped samples confirmed the XRD observation that the structural integrity of the samples is preserved under moderate doping concentrations. Figure 1c depicts the optimized structures of β-Ga_2O_3 and Sn_x-Ga_2O_3 derived from DFT calculations. The Sn_x-Ga_2O_3 structure was modeled by replacing a single Ga atom from the [100] surface with an Sn atom. A $1 \times 2 \times 4$ supercell of β-Ga_2O_3 was used for the calculations, and the calculated lattice parameter was 12.452 Å, which is consistent with other works.[46–48] Additionally, we found that the average bond length of Sn–O

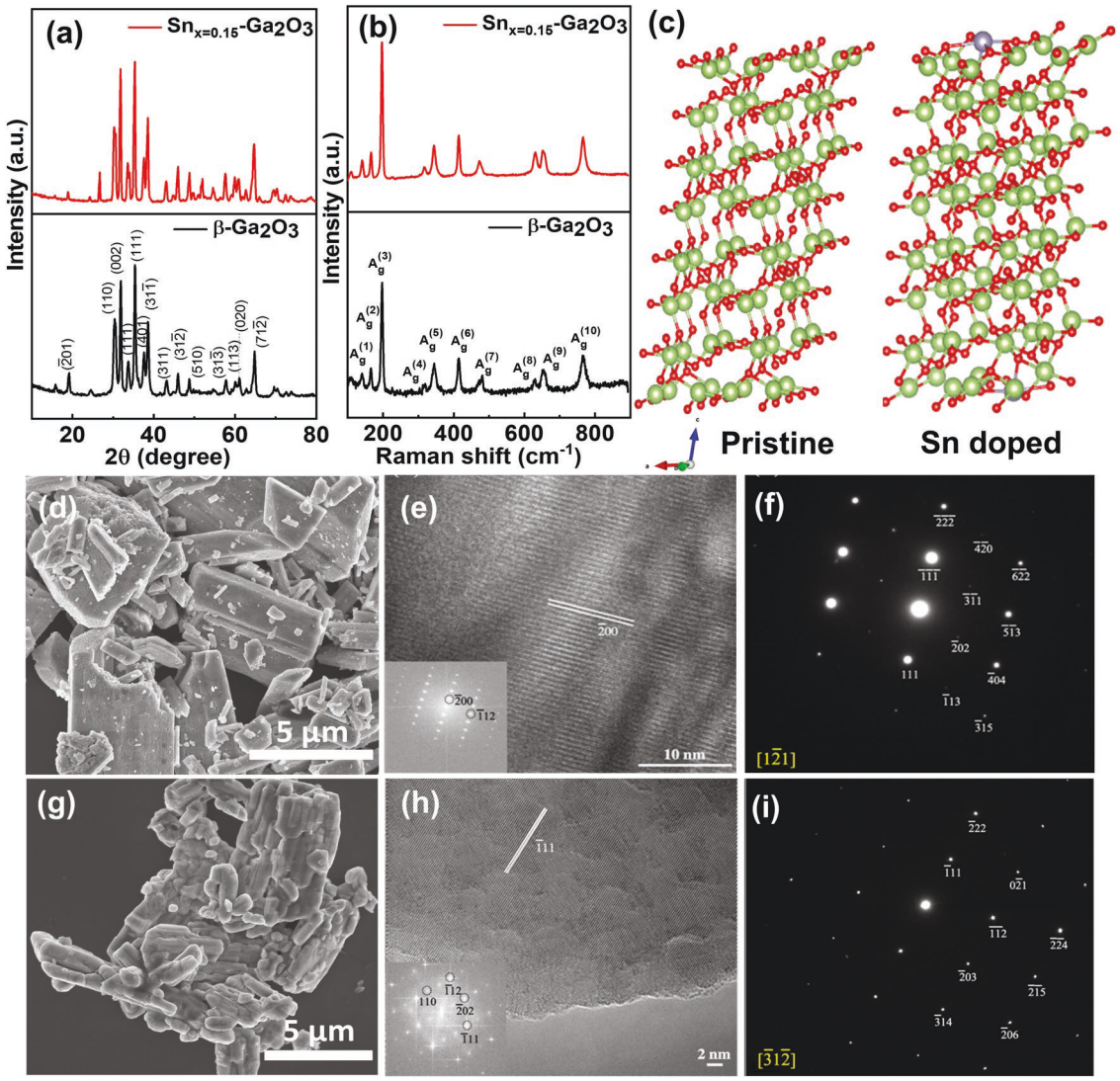

Figure 1. a) XRD spectrum, b) Raman spectrum, c) optimized structures of β-Ga_2O_3 (left), and Sn-doped β-Ga_2O_3 (right). d) SEM image of β-Ga_2O_3 and e) high-resolution TEM image for β-Ga_2O_3 (with -200 plane resolved) corresponding Fourier transform shown in the inset. f) SAED pattern for β-Ga_2O_3, g) SEM image of $Sn_{x=0.15}$-Ga_2O_3 (h) high-resolution TEM images for $Sn_{x=0.15}$-Ga_2O_3 showing a -111 plane; corresponding Fourier transform shown in the inset i) SAED pattern for $Sn_{x=0.15}$-Ga_2O_3.

(2.14 Å) is greater than Ga–O (1.81 Å), which corresponds to the larger atomic radius of Sn^{4+} (0.70 Å) compared to Ga^{4+} (0.62 Å). Moreover, the calculated reduction in the bandgap upon Sn doping using DFT is well consistent with the literature.[49,50] The morphology of β-Ga_2O_3 and $Sn_{x=0.15}$-Ga_2O_3 and the lattice structure were studied using scanning electron microscopy (SEM) and transmission electron microscopy (TEM). The SEM micrograph (Figure 1d,g) validates the bulk powder nature of β-Ga_2O_3 as well as $Sn_{x=0.15}$-Ga_2O_3. It is evident that the rod-shaped nature of monoclinic β-Ga_2O_3 is mostly preserved with the introduction of Sn dopant into the lattice. Elemental analysis performed using energy-dispersive X-ray spectrometry (EDS) confirmed the presence of Ga, O, and Sn elements in $Sn_{x=0.15}$-Ga_2O_3 (Figure S3, Supporting Information). Our X-ray photoelectron spectroscopy (XPS) analysis further confirmed the Sn doping. Figure S4, Supporting Information shows the Ga 2p, Sn 3p, and Sn 3d high resolution XPS spectrum for Ga_2O_3 samples with $x = 0$ and $x = 0.15$ dopant percentages. The high-resolution XPS analysis in the Ga 2p region indicates that Ga exists in a +3 oxidation state in both the samples. Similarly, the oxidation state of Sn was also confirmed to be +4.

To probe the atomic-level crystal structure (and validate our DFT calculations) and understand any lattice distortions or formation of interfacial compounds during Sn doping, we analyzed our sample using high-resolution TEM (HRTEM). Figure 1e,f,h,i show lattice resolved TEM image and selected area electron diffraction (SAED) of pure β-Ga_2O_3 and $Sn_{0.15}$-Ga_2O_3 samples. The HRTEM image in Figure 1e shows the 002 planes confirming the monoclinic structure of pure β-Ga_2O_3. The corresponding SAED pattern (Figure 1f) and the FFT pattern (inset of Figure 1e) confirmed the highly crystalline monoclinic phase of the sample. Interestingly, the $Sn_{x=0.15}$-Ga_2O_3

also exhibited a 111 plane (Figure 1h), and the crystalline nature in the SAED (Figure 1i) and the FFT (inset of Figure 1h), again emphasizing that the crystal structure is mostly preserved in samples up to $Sn_x = 0.15$. Thus, as established in our bulk XRD measurements,[39] the HRTEM and SAED analysis confirmed that no apparent change in the crystal structure or separation of secondary phases happened until $x \leq 0.15$, even at local nanoscopic levels. It is also evident that the segregation of dopants in the form of tetragonal SnO_2 can be observed only at higher doping concentrations.[39] It is interesting to note that, without any significant structural modifications, the doping resulted in substantial changes in the electronic structure, and the bandgap of doped samples varied in the range of 4.7–4.5 eV (Figure S5, Supporting Information), with an inverse relationship between the amount of Sn-doping and the bandgap.[39]

2.2. Electrocatalytic Activity

Linear sweep voltammetry (LSV) measurements using a rotating disk electrode (RDE) in O_2 saturated 0.1 M KOH solution were performed to investigate the ORR activity of bulk β-Ga_2O_3 and Sn_x-Ga_2O_3 samples. The presence of a reduction peak in the ORR region after O_2 saturation and the absence of any such peak in N_2 saturated electrolyte indicates the intense ORR activity of the as-synthesized materials (Figure S6, Supporting Information). As evident from **Figure 2**a, the performance improved with increasing the doping ratio up to 15%, beyond which the limiting current decreased. Compared to other dopant ratios, the $Sn_{x=0.15}$-Ga_2O_3 sample displayed an exceptional ORR activity with an onset potential of 0.76 V and half-wave potential ($E_{1/2}$) of 0.7 V, which is one of the best reported for any Ga_2O_3-based materials. Thus, the LSV curves proved that doping of Sn enhances the ORR activity of pristine β-Ga_2O_3 (onset 0.6 V vs RHE). The ORR activity of pristine SnO_2 revealed a poor activity thereby confirming the importance of a doping-based strategy to enhance ORR (Figure S7, Supporting Information). Figure 2b shows the mass activity obtained from the ORR polarization curve of the $Sn_{x=0.15}$-Ga_2O_3 at 0.6 V and is found to be 0.09 A mg^{-1} which is close to the benchmark Pt/C (0.11 A mg^{-1} with loading 50 μg cm^{-2} that of Pt/C). The oxygen reduction properties were further analyzed by varying rotation speeds ranging from 200 to 1600 rpm for Pt/C and $Sn_{x=0.15}$-Ga_2O_3 (Figure 2c,d). From the RDE voltammograms, the limiting current of ORR on $Sn_{x=0.15}$-Ga_2O_3 increased with increasing rotation speed from 200 to 1600 rpm, illustrating first-order reaction kinetics (Figure 2d), with a maximum diffusion-limited current density of 4.5 mA cm^{-2} at 1600 rpm. The kinetic parameters were estimated by applying the Koutecky–Levich (K–L) equations. The linearity of the K–L plots for Pt/C and $Sn_{x=0.15}$-Ga_2O_3 (insets of Figure 2c,d) also confirms similar first-order reaction kinetics with respect to the dissolved oxygen concentration in the case of both the catalysts. We also investigated the mechanism of ORR to understand

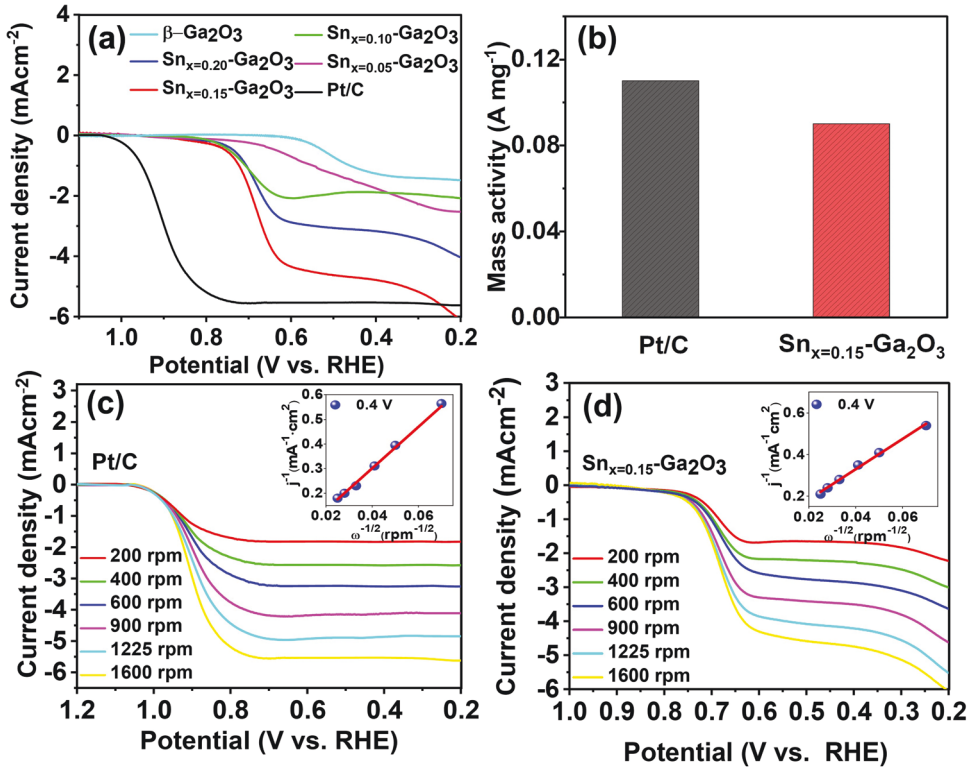

Figure 2. a) Linear sweep voltammetry of the Ga_2O_3 and Sn_x-Ga_2O_3 with different ratios (electrode-rotating speed, 1600 rpm. Scan rate: 2 mV s^{-1}). b) Mass activity of $Sn_{x=0.15}$-Ga_2O_3 and Pt/C at 0.6 V versus RHE. c) The RDE plots of Pt/C in oxygen-saturated 0.1 M KOH at rotation speeds ranging from 200 to 1600 rpm and a scan rate of 10 mV s^{-1}. Inset (K–L plots). d) The RDE plots of $Sn_{x=0.15}$-Ga_2O_3 in oxygen-saturated 0.1 M KOH at rotation speeds ranging from 200 to 1600 rpm and a scan rate of 10 mV s^{-1}. Inset (K–L plots).

whether it proceeds through four electrons or two electrons pathway.[51–53] The kinetic parameters obtained from K–L plots demonstrated that Pt/C under dynamic conditions exhibits a 3.8 electrons-based mechanism. The average electron transfer number for $Sn_{x=0.15}$-Ga_2O_3 was calculated to be 3.7 electrons, confirming that the mechanism follows a four-electron reduction process (Figure 2d inset).

In addition to ORR activity, bifunctional catalysts that can promote OER activity are beneficial for application as cathode material in high energy density devices such as the Zn-air battery. Hence to check the bifunctional nature, we investigated the electrocatalytic OER performance for the Sn_x-Ga_2O_3 system in an alkaline electrolyte (0.1 M KOH). **Figure 3**a shows the iR corrected CV curves with different Sn loading. Similar to the ORR activity, the CV curves showed a superior activity for $Sn_{x=0.15}$-Ga_2O_3 compared to other dopant ratios with an onset potential of 1.75 V versus RHE. Additionally, to understand the catalytic mechanism of the electrocatalytic OER process, we evaluated the Tafel slopes (Figure 3b). A smaller Tafel slope indicates superior catalytic efficacy and resultant increased OER rate, with decreased overpotentials.[54] A Tafel slope of 128 mV dec^{-1} for $Sn_{x=0.15}$-Ga_2O_3 again confirmed the superior OER performance of the 15% doped sample compared to other ratios.

To understand the origin of the superior performance of the doped electrocatalysts, we investigated the bandstructure, calculated the double-layer capacitance (C_{dl}), and analyzed the samples using electrochemical impedance spectroscopy (EIS). The band structure of the bulk β-Ga_2O_3 and Sn-doped Ga_2O_3 samples was explored using cyclic voltammetry (CV), and corresponding highest occupied molecular orbital (HOMO) and lowest unoccupied molecular orbital (LUMO) were identified (Figure S8, Supporting Information).[55,56] It is evident from the figure that the better proximity of HOMO with the oxygen reduction potential in $Sn_{x=0.15}$-Ga_2O_3 aids in enhanced electron transfer, thereby improving the reaction kinetics. Our EIS analysis demonstrated that $Sn_{x=0.15}$-Ga_2O_3 has the smallest charge transfer resistance among all the ratios (Figure 3c). Figure S9, Supporting Information and Figure 3d show the CV and C_{dl} plots, which indicate an increase in the electrochemical surface area with increased doping percentage (x = 0.05–0.20). Though a minimal rise in C_{dl} value (1.03 vs 1.18 $mFcm^{-2}$) is observed between $Sn_{x=0.15}$-Ga_2O_3 and $Sn_{x=0.2}$-Ga_2O_3, as evidenced by the EIS measurements, $Sn_{x=0.15}$-Ga_2O_3 has the lower charge transfer resistance (Figure 3d) compared to $Sn_{x=0.2}$-Ga_2O_3, potentially leading to the superior bifunctional activity of $Sn_{x=0.15}$-Ga_2O_3 towards ORR and OER. The turnover frequency (TOF) reveals the intrinsic efficiency, by calculating the rate of product formation (O_2) at a specific catalytic site.[57] To calculate TOF, the number of Sn active sites in the sample was calculated from inductively coupled plasma optical emission spectrometer (ICP–OES) measurements (Table S1, Supporting Information). The TOF of $Sn_{x=0.15}$-Ga_2O_3 on Sn active sites was calculated to be 0.88 s^{-1} at a current density of 10 $mAcm^{-2}$. To evaluate the efficiency of the catalyst towards OER, we also calculated the Faradaic efficiency (F.E). For this, the amount of oxygen generated from OER was calculated using gas chromatography. Subsequently, the experimental yield was compared with the

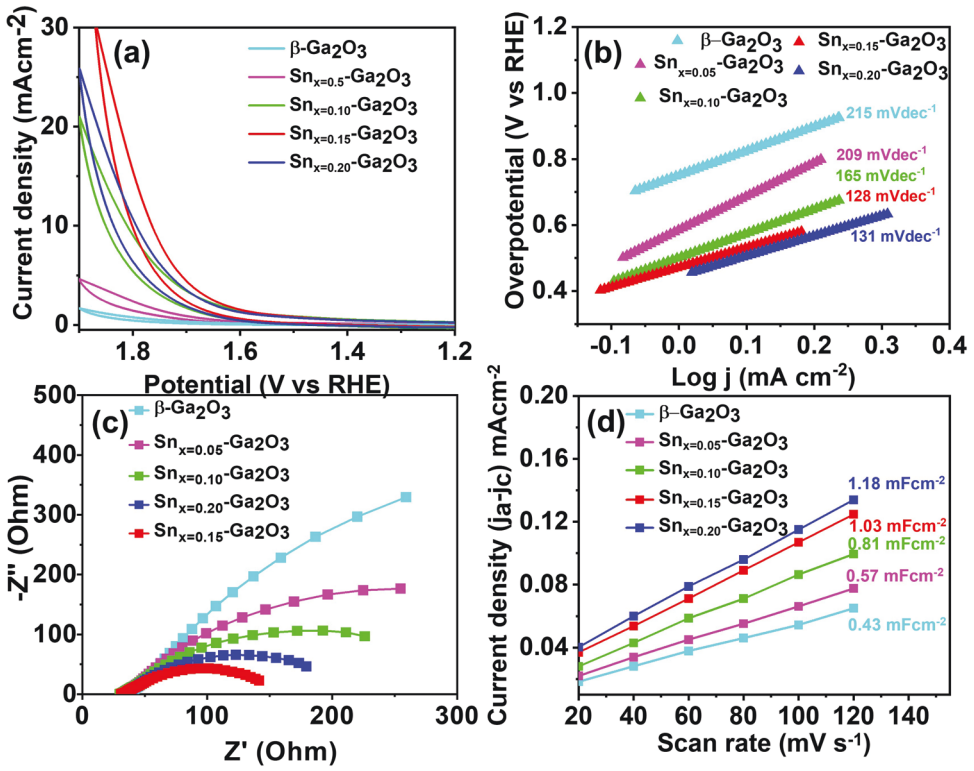

Figure 3. a) iR corrected CV measurements for OER and b) corresponding Tafel plot. c) Nyquist plot and d) C_{dl} measurements for β-Ga_2O_3 and Sn_x-Ga_2O_3 systems.

theoretically expected values to calculate the FE. Our analysis gave a Faradaic efficiency of 98% for $Sn_{x=0.15}$-Ga_2O_3, further indicating its catalytic activity towards OER (Figure S10, Supporting Information). Hence, our experimental exploration suggests that in $Sn_{x=0.15}$-Ga_2O_3, the proximity of HOMO to oxygen reduction potential, a lower charge transfer resistance, and higher electrochemical surface area, work synergistically to enhance electrocatalytic activity and selectivity compared to the other dopant ratios. Table S2, Supporting Information compares the OER and ORR activity of $Sn_{x=0.15}$-Ga_2O_3 with other reported works in the literature. Compared to other reported systems, the performance of the $Sn_{x=0.15}$-Ga_2O_3 doped sample is superior or comparable, despite being largely bulk in nature.

To gather a comprehensive understanding of the ORR and OER mechanism of β-Ga_2O_3 and Sn-doped β-Ga_2O_3 samples and identify the active sites on the doped materials, we performed DFT calculations. Our DFT-based analysis concentrated on the adsorption behavior of reactants (O_2), intermediates (OOH *, O*, and OH*), and products (H_2O) in an alkaline medium. The exposed planes for the calculations were selected based on the previous reports which indicated that [100] planes have the lowest surface formation energy, electrocatalytic efficiency, and enhanced optical properties.[58–60] Initially, we employed the electron localization function (ELF) to investigate the electron distribution on the surface of β-Ga_2O_3 and Sn-doped Ga_2O_3. The ELF can be described as a contour plot in real space, as shown in Figures 4a,b. The region close to 0 (red) indicates a low electron density area, while a region close to 5 (blue) indicates a highly localized dense electron region coming from the nucleus or because of the presence of strong covalent electrons or lone-pair electrons. It is plausible that the dense electron accumulation on the Sn atom site arises due to the electron donation from the adjacent Lewis acid sites to the Sn–O bond. This observed electron accumulation on the Sn site is anticipated to exhibit stronger covalent interactions with the ORR and OER intermediates. For ORR and OER, the catalytic activity of the studied substrates in the alkaline medium mainly depends upon the initial adsorption of O_2 followed by the adsorption energies of various reaction intermediates. The Gibbs free energy diagram calculated using the standard $4e^-$ association mechanism is used to study the bifunctional ORR and OER activity on β-Ga_2O_3 and Sn-doped Ga_2O_3 substrates. We examined two kinds of adsorption patterns: end on and side on for initial O_2 adsorption and observed that the end-on configuration is more energetically favorable for both β-Ga_2O_3 and Sn-doped Ga_2O_3 substrates. To confirm the active sites on the catalyst, we investigated various possible adsorption sites for the reaction intermediates (OOH*, O*, and OH*) on the substrates. The most stable structural configurations are shown in Figure S11, Supporting Information, which validates that Sn is the most active site in Sn-doped Ga_2O_3, whereas it is the Ga site in β-Ga_2O_3. The corresponding reaction free energies for each intermediate step in ORR are shown in **Figure 4**c. From the calculations, we confirmed that the rate-determining step (RDS) is the fourth hydrogenation step ($4OH^-$), with the highest energy barrier[61] corresponding to the stronger or weaker binding energies between the oxygenated species and substrates. For the overall ORR reaction at U = 0 V, the rate-determining step for β-Ga_2O_3 is O*→ OH* (2.216 eV), whereas for Sn-doped Ga_2O_3, the RDS is OH* → OH^- (1.899 eV). It is worth mentioning that Sn-doped Ga_2O_3 requires less energy to make all the reaction intermediate steps to be thermodynamically downhill, revealing its superior ORR activity compared to the parent substrate. Moreover, the initial oxygen adsorption step is thermodynamically uphill for pristine Ga_2O_3. In contrast, Sn doping significantly reduces the energy barrier, making the O_2 adsorption thermodynamically downhill and is well correlated with its stronger adsorption energies and increased charge transfer characteristics. Further, for Sn-doped Ga_2O_3, we found electron-dense clouds around incoming O atoms confirming the charge transfer from the metal atoms to incoming O atoms (Figure S12, Supporting Information).

We performed Bader charge analysis to establish the increased electron density in Sn-doped Ga_2O_3 and electron transfer from Lewis sites (Figure 4d). The Lewis acid coordination in Sn-doped Ga_2O_3 allows for electron transfer from the Ga^{3+} to the Sn–O bond, facilitating the formation of intermediates in ORR and OER. The increased electron charge transfer values in the case of Sn-doped Ga_2O_3 substrates for all the intermediate steps in ORR and OER also confirmed the charge transfer. Also, as per the Bader charge calculation, the formation of the O* intermediate is enhanced the most due to the strong Lewis acid property of the system. We also observed that while the average charges of Ga and O atoms for the O* intermediate are 1.799 and −0.481|e|, the charges are 2.271 |e| for Sn and −0.541 |e| for O in Sn-doped Ga_2O_3, again pointing to the higher charge transfer characteristics of Sn-doped substrate. Additionally, a charge density difference analysis was performed to establish the increased chemical interaction between the metal p orbital and π^* antibonding orbital of O_2. We found a ≈2.5% and ≈7% increase in the O–O bond lengths (Figure 4e and Figure S13, Supporting Information) for the β-Ga_2O_3 and Sn-doped Ga_2O_3 compared to the corresponding gas-phase molecule ($d_{O=O}$ = 1.22 A^o). This is because there is a higher charge transfer of ≈0.89 |e| from Sn to O_2 in Sn-doped Ga_2O_3, compared to ≈0.77 |e| from Ga to O_2, corroborating the increased elongation of the O=O bond length (Figure 4e and Figure S13, Supporting Information). Charge density difference analysis performed on O_2 adsorbed substrates also reveals a charge accumulation between Sn–O bonds indicating stronger covalent interactions. Hence, experimentally observed superior ORR activity of Sn-doped Ga_2O_3 agrees with theoretical DFT calculations. Moreover, the calculated theoretical overpotential of Sn-doped Ga_2O_3 was lower (0.66 eV) when compared to that of pristine Ga_2O_3 (0.98 eV) illustrating that the Sn doping could improve the ORR catalytic activity than pristine Ga_2O_3. The enhancement in OER activity was also further proved using Gibbs free energy calculations. Figure 4f shows the proposed $4e^-$ mechanism for OER on β-Ga_2O_3 and Sn-doped Ga_2O_3 substrates. Like ORR, the OER on both β-Ga_2O_3 and Sn-doped Ga_2O_3 catalysts also proceeds in four elementary steps with the generation of OH*, O*, and OOH* as the OER intermediates. The computed free energy of each OER intermediate step takes place at corresponding metal sites in β-Ga_2O_3 and Sn-doped Ga_2O_3. From Figure 4g, we observed that the intermediate step involving the deprotonation of OH* to O* is the rate-determining step in the overall OER process. The computed difference in Gibbs free energy value of Sn-doped Ga_2O_3

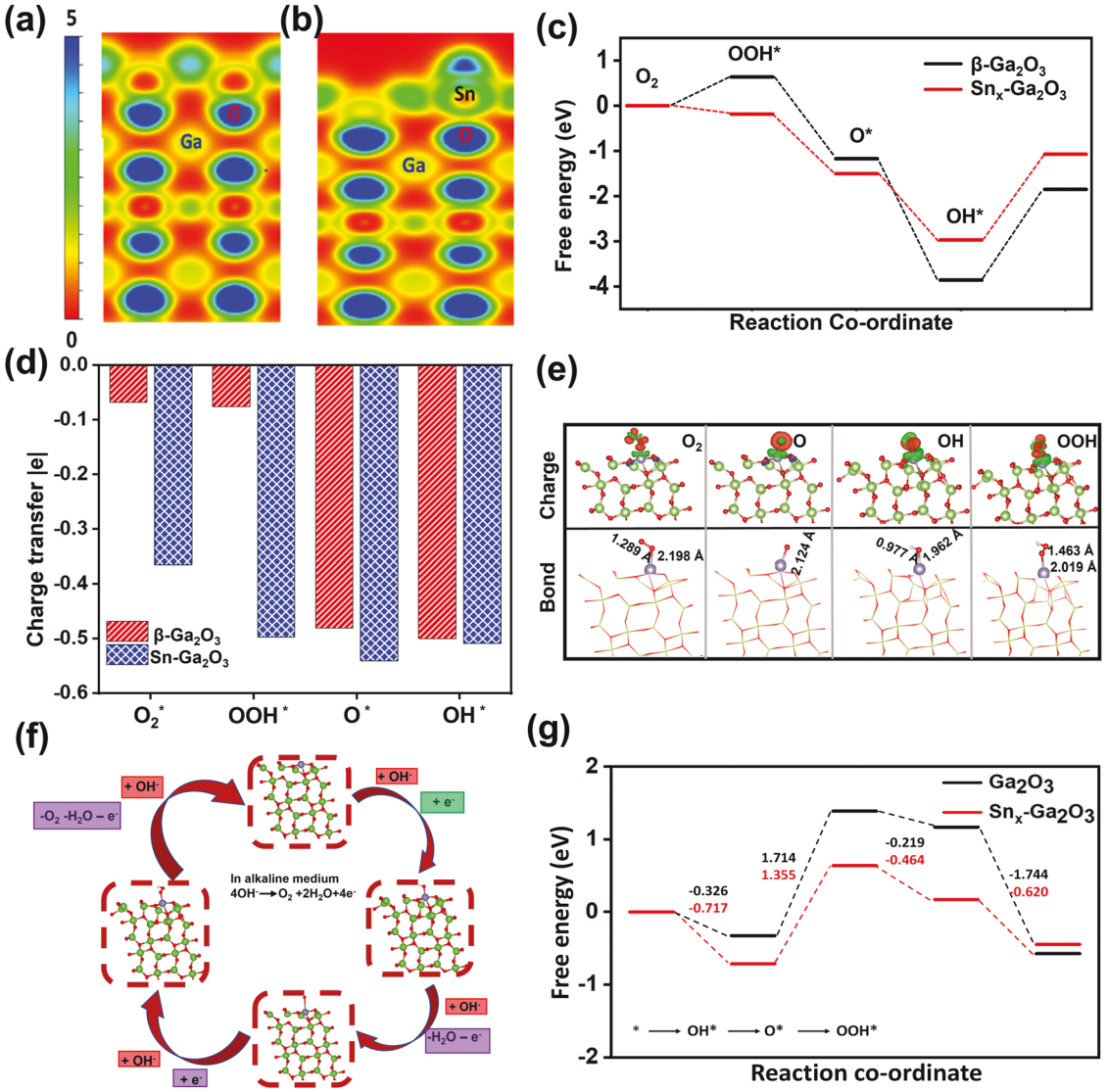

Figure 4. Electron localization function plots of a) β-Ga_2O_3 and b) Sn_x-Ga_2O_3. c) Gibbs free energy diagram for ORR. d) Bader charge calculation. e) Charge density difference analysis and bond length calculation for Sn_x-Ga_2O_3. f) Mechanism for OER. g) Gibbs free energy diagram for OER.

(1.355 eV) is much lower than the β-Ga_2O_3 (1.714 eV), indicating that lower overpotential is required for the Sn-doped catalyst to drive the water oxidation and thus higher theoretical OER activity.

2.3. Zn-Air battery

The superior bifunctional electrocatalytic activity of bulk $Sn_{x\,=\,0.15}$-Ga_2O_3 inspired us to construct a rechargeable Zn-air battery using the doped material as the cathode (**Figure 5**a). A solution of 6 M KOH with 0.2 M zinc acetate solution was used as the electrolyte. A charge-discharge cycle test was performed with a current density of 2 mA cm^{-2} on two separate devices using Pt/C + RuO_2 (benchmark) and $Sn_{x\,=\,0.15}$-Ga_2O_3 as air cathode (Figure 5b,c). As shown in Figure 5b (Figure S14, Supporting Information), the initial charge and discharge potentials of $Sn_{x\,=\,0.15}$-Ga_2O_3 (red curve) reached 1.80 and 1.22 V, respectively, whereas it was 1.81 and 1.19 V for Pt/C + RuO_2 (black curve) after 120 h. While $Sn_{x\,=\,0.15}$-Ga_2O_3 and commercial Pt/C and RuO_2 catalysts exhibited similar charging and discharging potential at low current density (Figure 5c), $Sn_{x\,=\,0.15}$-Ga_2O_3 has a smaller polarization at high current densities, indicating a better performance at high current densities for the Zn-air battery than the corresponding state-of-the-art battery based on Pt/C + RuO_2 mixture air-cathode. The increased polarization of Pt/C + RuO_2 compared to $Sn_{x\,=\,0.15}$-Ga_2O_3 causes a higher reduction in the performance of the battery. Further, no significant potential drop was observed during galvanostatic discharge for 24 h at 2 mA cm^{-2} (Figure S15, Supporting Information), indicating good catalytic stability of $Sn_{x\,=\,0.15}$-Ga_2O_3 in the metal-air battery. Figure 5d shows that the maximum power density of the Zn-air battery using the $Sn_{x\,=\,0.15}$-Ga_2O_3 catalyst was determined to be 138 mW cm^{-2}, close to that of

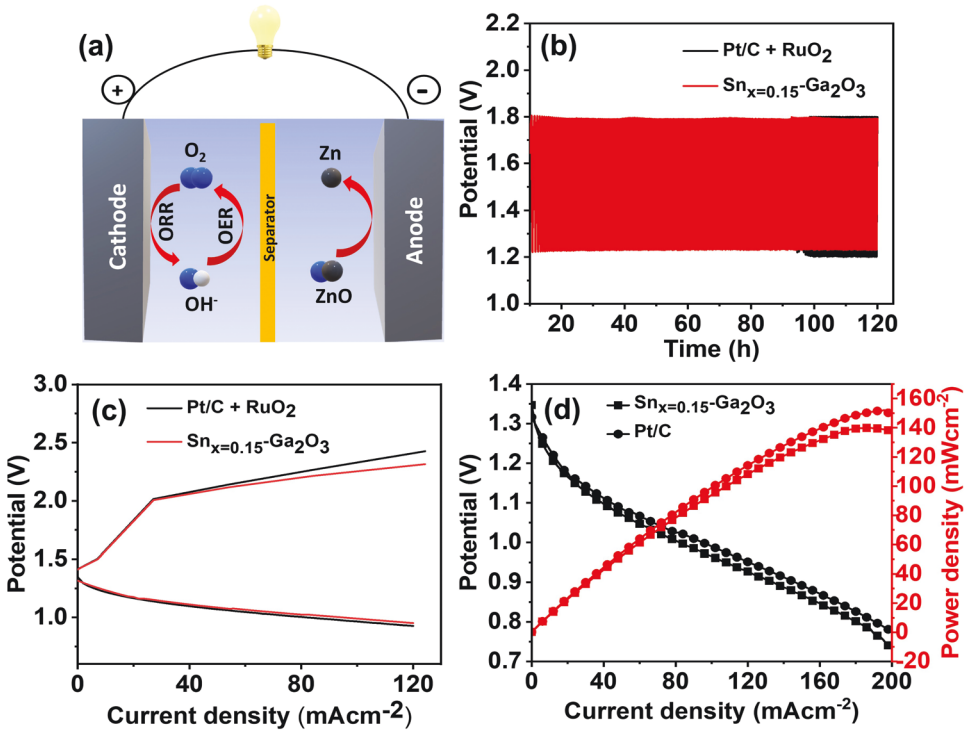

Figure 5. a) Schematic representation of Zn-air battery, b) charge-discharge cycles of $Sn_{x=0.15}$-Ga_2O_3 and Pt/C + RuO_2 mixture, c) charge and discharge cycle showing the polarization in $Sn_{x=0.15}$-Ga_2O_3 and Pt+RuO_2, and d) discharge cycle and power density values at different current densities for $Sn_{x=0.15}$-Ga_2O_3 and Pt/C.

the benchmark Pt/C + RuO_2 catalyst (150 mW cm^{-2}). Under a higher current density of 10 $mAcm^{-2}$, the battery charge–discharge cycles showed very low polarization and stable cycles for 30 h (Figure S16, Supporting Information). Therefore, the Sn-doped Ga_2O_3-based Zn-air battery showed comparable power performance and enhanced stability to the device with benchmark Pt/C + RuO_2 air-cathode. Our post-mortem OER, ORR, and Zn-air battery cycling characterizations of $Sn_{x\ =\ 0.15}$-Ga_2O_3 catalysts using SEM, XRD, Raman, and ICP–OES measurements (Figures S17–S19, and Table S1, Supporting Information) further confirmed the superior stability of the catalysts. As revealed by the characterizations, $Sn_{x\ =\ 0.15}$-Ga_2O_3 does not undergo any structural or chemical changes after electrochemical measurements pointing to their potential long-term utility.

3. Conclusion

In summary, we designed a bulk $Sn_{x\ =\ 0.15}$-Ga_2O_3 catalyst with superior bifunctional ORR and OER activity and durability in alkaline media. The excellent catalytic activity of Sn-doped Ga_2O_3 is attributed to the symbiotic relationship between Ga^{3+} Lewis acid sites and Sn-based active sites with favorable oxygen adsorption characteristics. The symbiotic relationship significantly improved the electronic density distribution around Sn, as confirmed by the electron localization function plots. Further, the Bader charge analysis established that the formation of the intermediates, especially the O*, was significantly improved due to the strong Lewis acid property of Sn-doped Ga_2O_3. Finally, $Sn_{x\ =\ 0.15}$-Ga_2O_3 was successfully employed as cathodes in Zn-air batteries, displaying the highest power density and excellent charge-discharge stability reported from a bulk system. The rational design of atomically dispersed Lewis acid sites in our study is beneficial for constructing high-performance bifunctional bulk electrocatalysts for electrochemical energy applications.

4. Experimental Section

Synthesis: The Sn mixed Ga_2O_3 compounds were produced via the high-temperature, solid-state chemical reaction method. To obtain the homogenous mixtures, high pure β-Ga_2O_3 and SnO_2 powders are mixed thoroughly. In the solid-state synthesis route adopted, the process was first initiated by grinding the powders using a mortar and pestle under a volatile liquid environment. This ensured the homogeneous mixing and formation of smaller size particles. The mixture was then heat treated and calcined, at a temperature closer to the melting point of the material. In this case, the mixed compound was heat treated at 1100 °C for 12 h in a muffle furnace. The ramp rate used for heating and cooling was 5 °C min^{-1}. After calcination of the sample, the mixture was ground again by introducing polyvinyl acetate (PVA). Under the presence of PVA, the mixture had been ground into a fine powder, which was then used to make pellets. The pellets were made by pressing the final Sn_x-Ga_2O_3 powder at 1.5 tons for 1 min. The pellets were made with an 8 mm diameter and 2 mm thickness. The second stage of compound synthesis involved the sintering process. The pellets were subjected to the second heat treatment, that is, sintering. The sintering temperature, which was typically higher than the calcination temperature, was set to 1350 °C for 12 h while maintaining the same ramp rate as in the calcination. The materials thus obtained were subjected to further characterization to understand the structure, composition, and electrochemical properties.

Material Characterization: The XRD analysis was performed on a Rigaku Smartlab diffractometer in 0D mode with HyPix 3000 high energy

resolution 2D HPAD detector. A trace amount of Sn_x-Ga_2O_3 powder was placed on a zero-diffraction plate to counter any diffraction peak arising from the sample holder. The X-ray source was set at the operating parameters of 44 kV and 40 mA. The step size was kept at 0.02 degrees. The diffraction data analysis or phase matching was carried out using proprietary PDXL software. The morphology of the Sn_x-Ga_2O_3 samples was studied using the FEI Magellan 400 scanning electron microscope. TEM samples were prepared by the simple drop cast method for powder samples. To remove agglomerates, the powder was sonicated for 10 s to achieve a homogeneous dispersion. Then a drop from the dilute solution of each aliquot was drop cast over an amorphous C-coated Cu grid. TEM studies were performed on a JEOL-Arm 200CF microscope operating at 200 kV equipped with a high dynamic range Gatan DIF camera for diffraction patterns. Total gallium and tin content in the GaSnO compounds were determined using an inductively coupled plasma optical emission spectrometer (ICP-OES, Perkin-Elmer Optima 4300 DV, Shelton, CT). A calibrated Kratos Axis Ultra DLD spectrometer (Kratos Analytical, Manchester, U.K.) which has a high-performance Al Kα (1486.7 eV) spherical mirror analyzer was used for XPS analysis. Gas detection and quantitative analysis were performed by a SHIMADZU GC-8A gas chromatograph (GC)

Electrochemical Measurements: The electrocatalytic performance of all catalysts was analyzed by CV, LSV, and chronoamperometric test using a CHI6372E CH instrument workstation. The electrochemical workstation was coupled with a rotating disk electrode (Pine Research) system. All the experiments were performed in a three-electrode configuration using platinum wire as a counter electrode, a saturated calomel electrode (SCE) as a reference electrode, and a glassy carbon electrode having a 3 mm diameter as a working electrode.[62,63] The electrolyte used was a 0.1 M aqueous KOH solution. All potentials reported in this work were calibrated versus the reversible hydrogen electrode (RHE) using the equation,

$$E(RHE) = E(SCE) + (0.197 + 0.059 * pH) \quad (1)$$

The OER activity was obtained via CV at a low scan rate of 5 mV s^{-1}. The overpotential values corresponding to different current densities were determined from the cathodic going half cycle of the CV curves. The voltammograms were recorded with 90% iR drop compensation automatically on the workstation, where the potential and current offset were measured and compensated.[64] The ohmic resistance was corrected according to E = E(RHE)-iR, where *E* is the iR-corrected potential, E(RHE) is the measured potential with respect to RHE, *i* is the measured current, and *R* is the uncompensated resistance. The capacitance of the catalytic surface was measured from the non-Faradaic capacitive current associated with double layer charging from the scan rate dependence of cyclic voltammograms. Cyclic voltammograms were recorded in a non-Faradaic region at various scan rates.[65–68]

For the Zn-air battery test, the air electrode was prepared by uniformly coating the as-prepared catalyst ink onto a glassy carbon working electrode and then drying it at room temperature. The mass loading was 4 mg cm^{-2} unless otherwise noted. A Zn foil was used as the anode. Both electrodes were assembled into a Zn-air battery setup and a 6 M KOH (pH 13.78) aqueous solution with 0.2 M zinc acetate solution was used as the electrolyte. Further, a potential versus current density graph was plotted for Pt/C + RuO_2 and $Sn_{x=0.15}$-Ga_2O_3. For this, individual charge and discharge measurements were performed at various current densities. Data points corresponding to different voltages were selected and plotted together.

Faradaic Efficiency Calculation: Chronoamperometry measurement was performed in a gastight electrochemical two compartment H-cell using Pt wire and Hg/HgO as the counter electrode and the reference electrode, respectively. The working electrode and reference electrode were placed in the anode cell and the counter electrode was put in the cathode cell. 50 mL 0.1 M KOH aqueous solution was used as an electrolyte. Before the measurements, the solution was purged with Argon gas for 30 min to completely remove the oxygen gas in the system. The generated O_2 volume during electrolysis was measured using gas chromatography. Faradaic efficiency (F.E) was calculated using the equation,

$$F.E = \frac{Experimental\ moles\ of\ \ Oxygeng\ as}{Theoretical\ moles\ of\ \ Oxygeng\ as} \times 100 \quad (2)$$

The theoretical amount of O_2 gas was calculated from Faraday's law,

$$n = \frac{iXt}{zXF} \quad (3)$$

where *n* is the number of moles, *i* is the current in ampere, *t* is the time in seconds, *z* is the transfer of electrons (for O_2 z = 4), and *F* is the Faraday constant (96 485 C mol^{-1}).

Calculation of TOF: The turnover frequency was defined as moles of O_2 per moles of the active site (Sn) evolved per s (s^{-1}). The geometric current densities (*j*) were extracted at 520 mV overpotential (1.75 V RHE, all reported potentials are iR corrected) from CV measurements. The total moles of Sn on the electrode was determined by ICP–OES prior to the measurement. *A* is the area of the GC electrode surface (3 mm diameter). Assuming a *z* = 4 electron transfer for the overall reaction, TOF was calculated according to the equation below,

$$TOF = \frac{jXA}{4XFXn} \quad (4)$$

Computational Methods: The Vienna Ab initio Simulation Package was used for all spin-polarized DFT computations (VASP).[69] To examine electron–electron exchange correlations, the projector augmented wave (PAW) approach was used to characterize the electron–ion interaction and the Perdew–Burke–Ernzerhof (PBE) functional with generalized gradient approximations. The van der Waal (vdW) interactions for the substrates were described using Grimme's DFT-D3 technique. For the plane-wave (PW) basis computations, a kinetic cutoff energy of 520 eV was employed. With the addition of 20 A^0 vacuum space along the z-axis, the interaction between two nearby images was avoided. To examine the position of atoms and cell parameters, the conjugated gradient approach was used. For self-consistent electronic energy calculations, the convergence requirements were established at 10^{-4} eV in energy and 10^{-2} eV/in force. The Brillouin zone was sampled using a $5 \times 5 \times 1$ and $11 \times 11 \times 1$ k-point mesh generated using the Monkhorst–Pack scheme for both geometric and electronic relaxations. The charge transfer during the ORR (OER) intermediate adsorption was determined using Bader charge analysis, and charge differences were calculated using the formula

$$\rho_b = \rho_{\text{adsorbed state}} - (\rho_{\text{adsorbent}} + \rho_{AM}) \quad (5)$$

where $\rho_{\text{adsorbed state}}$, $\rho_{\text{adsorbent}}$, and ρ_{AM} represent the charge density of the pristine and Sn-Ga_2O_3 (AM) with adsorbed ORR (OER) intermediate species, pristine ORR(OER) species, and the AM, respectively. A VESTA code was used to analyze the charge density difference.[70]

The binding energies of the ORR(OER) intermediate species with the substrates were calculated using the expression,

$$\Delta E = E_{ads/sub} - E_{ads} - E_{sub} \quad (6)$$

where $E_{ads/sub}$, E_{ads}, and E_{sub} denotes the total energies for adsorbed species on substrate, adsorbed species and isloted substrate (AM) respectively.

The Gibbs free energy (ΔG) for each ORR (OER) intermediate step in the overall ORR (OER) process was calculated as

$$\Delta G = \Delta E + \Delta ZPE - T\Delta S + \Delta G_U + \Delta G_{pH} \quad (7)$$

where ΔE is for adsorption energy, ΔZPE and $T\Delta S$ stand for the zero-point energy difference and entropy difference between the gas and adsorbed phases obtained from frequency calculations at 298.15 K, and ΔG_U stands for the applied electrode potential contribution (U). $\Delta GpH = k_BT \ln 10$ pH, where T = 300 K and k_B is the Boltzmann

constant. For the acidic medium, pH = 0 was assumed and for the alkaline medium, pH = 14.

Supporting Information

Supporting Information is available from the Wiley Online Library or from the author.

Acknowledgements

The authors thank Dr. Louis Echegoyen for providing access to the Rotating Disk Electrode setup. S.T.S. acknowledges support from UTEP start-up grant and UT STARs award. S.T.S. and C.V.R. gratefully acknowledge support from the National Science Foundation (NSF) through NSF-PREM grant (#DMR-1827745). S.T.S. and C.V.R. also acknowledge the partial support from DOE under grant # DE-FE0031908. A portion of this research was performed on a project award (10.46936/cpcy.proj.2021.60259/60008213) from the Environmental Molecular Sciences Laboratory, a DOE Office of Science User Facility sponsored by the Biological and Environmental Research program under Contract No. DE-AC05-76RL01830 and also funded in part by a grant from the Washington State Department of Commerce's Clean EnergyFund.

Conflict of Interest

The authors declare no conflict of interest.

Data Availability Statement

The data that support the findings of this study are available from the corresponding author upon reasonable request.

Keywords

gallium oxide, Lewis acid sites, oxygen evolution reaction, oxygen reduction reaction, Zn-air batteries

Received: April 28, 2022
Published online: July 28, 2022

[1] X. Zhang, X.-G. Wang, Z. Xie, Z. Zhou, *Green Energy Environ.* **2016**, *1*, 4.
[2] J. S. Lee, S. Tai Kim, R. Cao, N. S. Choi, M. Liu, K. T. Lee, J. Cho, *Adv. Energy Mater.* **2011**, *1*, 34.
[3] Y. Li, J. Lu, *ACS Energy Lett.* **2017**, *2*, 1370.
[4] F. Cheng, J. Chen, *Chem. Soc. Rev.* **2012**, *41*, 2172.
[5] L. Zhang, X. Yang, R. Cai, C. Chen, Y. Xia, H. Zhang, D. Yang, X. Yao, *Nanoscale* **2019**, *11*, 826.
[6] Y. Li, H. Dai, *Chem. Soc. Rev.* **2014**, *43*, 5257.
[7] X. Cai, L. Lai, J. Lin, Z. Shen, *Mater. Horiz.* **2017**, *4*, 945.
[8] B. Prakoso, M. A. A. Mahbub, M. Yilmaz, I. G. Wenten, A. D. Handoko, A. Sumboja, *ChemNanoMat* **2021**, *7*, 354.
[9] C. Goswami, K. K. Hazarika, P. Bharali, *Mater. Sci. Energy Technol.* **2018**, *1*, 117.
[10] L. Wei, E. H. Ang, Y. Yang, Y. Qin, Y. Zhang, M. Ye, Q. Liu, C. C. Li, *J. Power Sources* **2020**, *477*, 228696.
[11] K. B. Ibrahim, M. C. Tsai, S. A. Chala, M. K. Berihun, A. W. Kahsay, T. A. Berhe, W. N. Su, B. J. Hwang, *J. Chin. Chem. Soc.* **2019**, *66*, 829.
[12] X. Zhang, C.-L. Dong, Z. Diao, Y.-R. Lu, S. Shen, *EcoMat* **2019**, *1*, 12005.
[13] H.-Y. Wang, Y.-Y. Hsu, R. Chen, T.-S. Chan, H. M. Chen, B. Liu, *Adv. Energy Mater.* **2015**, *5*, 1500091.
[14] M. W. Louie, A. T. Bell, *J. Am. Chem. Soc.* **2013**, *135*, 12329.
[15] M. M. Shahid, P. Rameshkumar, W. J. Basirun, J. C. Juan, N. M. Huang, *Electrochim. Acta* **2017**, *237*, 61.
[16] Y. Liang, Y. Li, H. Wang, J. Zhou, J. Wang, T. Regier, H. Dai, *Nat. Mater.* **2011**, *10*, 780.
[17] Q. Hong, H. Lu, J. Wang, *ACS Sustainable Chem. Eng.* **2017**, *5*, 9169.
[18] A. Zhao, J. Masa, W. Xia, A. Maljusch, M.-G. Willinger, G. Clavel, K. Xie, R. Schlögl, W. Schuhmann, M. Muhler, *J. Am. Chem. Soc.* **2014**, *136*, 7551.
[19] N. Bhandary, P. P. Ingole, S. Basu, *Int. J. Hydrogen Energy* **2018**, *43*, 3165.
[20] Q. Yang, W. Xu, S. Gong, G. Zheng, Z. Tian, Y. Wen, L. Peng, L. Zhang, Z. Lu, L. Chen, *Nat. Commun.* **2020**, *11*, 1.
[21] F. A. Carey, R. J. Sundberg, *Advanced Organic Chemistry: Part A: Structure and Mechanisms*, 5th ed., Springer, Boston, MA **2007**.
[22] M. R. Delgado, C. O. Areán, *Mater. Lett.* **2003**, *57*, 2292.
[23] C.-T. Shao, W.-Z. Lang, X. Yan, Y.-J. Guo, *RSC Adv.* **2017**, *7*, 4710.
[24] K. Nakagawa, M. Okamura, N. Ikenaga, T. Suzuki, K. Nakagawa, M. Okamura, T. Suzuki, T. Kobayashi, T. Kobayashi, *Chem. Commun.* **1998**, *9*, 1025.
[25] A. Kakoria, B. Devi, A. Anand, A. Halder, R. R. Koner, S. Sinha-Ray, *ACS Appl. Nano Mater.* **2018**, *2*, 64.
[26] T. Liu, Z. Feng, Q. Li, J. Yang, C. Li, M. Dupuis, *Chem. Mater.* **2018**, *30*, 7714.
[27] Y. Sun, X. Li, T. Zhang, K. Xu, Y. Yang, G. Chen, C. Li, Y. Xie, *Angew. Chem.* **2021**, *133*, 21745.
[28] J. Swaminathan, A. B. Puthirath, M. R. Sahoo, S. K. Nayak, G. Costin, R. Vajtai, T. Sharifi, P. M. Ajayan, *ACS Appl. Mater. Interfaces* **2019**, *11*, 39706.
[29] H. Feng, L. Tang, G. Zeng, J. Yu, Y. Deng, Y. Zhou, J. Wang, C. Feng, T. Luo, B. Shao, *Nano Energy* **2020**, *67*, 104174.
[30] J. Wang, T. Liao, Z. Wei, J. Sun, J. Guo, Z. Sun, *Small Methods* **2021**, *5*, 2000988.
[31] M. Bandi, V. Zade, S. Roy, A. N. Nair, S. Seacat, S. Sreenivasan, V. Shutthanandan, C. G. Van de Walle, H. Peelaers, C. V. Ramana, *Cryst. Growth Des.* **2020**, *20*, 1422.
[32] B. Mallesham, S. Roy, S. Bose, A. N. Nair, S. Sreenivasan, V. Shutthanandan, C. V. Ramana, *ACS Omega* **2020**, *5*, 104.
[33] G. Gutierrez, E. M. Sundin, P. G. Nalam, V. Zade, R. Romero, A. N. Nair, S. Sreenivasan, D. Das, C. Li, C. V. Ramana, *J. Phys. Chem. C* **2021**, *125*, 20468.
[34] J. T. Feaster, C. Shi, E. R. Cave, T. Hatsukade, D. N. Abram, K. P. Kuhl, C. Hahn, J. K. Nørskov, T. F. Jaramillo, *ACS Catal.* **2017**, *7*, 4822.
[35] A. Dutta, M. Rahaman, N. C. Luedi, M. Mohos, P. Broekmann, *ACS Catal.* **2016**, *6*, 3804.
[36] Y. Ling, G. Wang, D. A. Wheeler, Zhang, Y. Li, *Nano Lett.* **2011**, *11*, 2119.
[37] L. Sun, C. Han, T. Zhang, H. Zhu, X. Xia, L. Li, *Mater. Sci. Semicond. Process.* **2020**, *110*, 104935.
[38] N.-I. Kim, Y. J. Sa, S.-H. Cho, I. So, K. Kwon, S. H. Joo, J.-Y. Park, *J. Electrochem. Soc.* **2016**, *163*, F3020.
[39] G. Gutierrez, E. M. Sundin, P. G. Nalam, V. Zade, R. Romero, A. N. Nair, S. Sreenivasan, D. Das, C. Li, C. Ramana, *J. Phys. Chem. C* **2021**, *125*, 20468.
[40] B. Mallesham, S. Roy, S. Bose, A. N. Nair, S. Sreenivasan, V. Shutthanandan, C. V. Ramana, *ACS Omega* **2019**, *5*, 104.
[41] C. Ramana, S. Roy, V. Zade, A. K. Battu, N. Makeswaran, V. Shutthanandan, *J. Phys. Chem. Solids* **2021**, 110174.

[42] Y. Yao, Y. Ishikawa, Y. Sugawara, *J. Appl. Phys.* **2019**, *126*, 205106.
[43] C. Kranert, C. Sturm, R. Schmidt-Grund, M. Grundmann, *Sci. Rep.* **2016**, *6*, 1.
[44] A. Khan, S. N. Khan, W. Jadwisienczak, M. E. Kordesch, *Sci. Adv. Mater.* **2009**, *1*, 236.
[45] Y. Wang, N. Li, P. Duan, X. Sun, B. Chu, Q. He, *J. Nanomater.* **2015**, *2015*, 191793.
[46] S. Kumar, R. Singh, *Phys. Status Solidi RRL* **2013**, *7*, 781.
[47] J. Åhman, G. Svensson, J. Albertsson, *Acta Crystallogr. C* **1996**, *52*, 1336.
[48] C. Janowitz, V. Scherer, M. Mohamed, A. Krapf, H. Dwelk, R. Manzke, Z. Galazka, R. Uecker, K. Irmscher, R. Fornari, M. Michling, D. Schmeißer, J. R. Weber, J. B. Varley, C. G. V. de Walle, *New J. Phys.* **2011**, *13*, 085014.
[49] Y. Zhang, J. Yan, G. Zhao, W. Xie, *Phys. B* **2010**, *405*, 3899.
[50] H. Ryou, T. H. Yoo, Y. Yoon, I. G. Lee, M. Shin, J. Cho, B. J. Cho, W. S. Hwang, *ECS J. Solid State Sci. Technol.* **2020**, *9*, 045009.
[51] S. Xu, Y. Kim, D. Higgins, M. Yusuf, T. F. Jaramillo, F. B. Prinz, *Electrochim. Acta* **2017**, *255*, 99.
[52] A. Kulkarni, S. Siahrostami, A. Patel, J. K. Nørskov, *Chem. Rev.* **2018**, *118*, 2302.
[53] X. Ge, A. Sumboja, D. Wuu, T. An, B. Li, F. T. Goh, T. A. Hor, Y. Zong, Z. Liu, *ACS Catal.* **2015**, *5*, 4643.
[54] A. Holewinski, S. Linic, *J. Electrochem. Soc.* **2012**, *159*, H864.
[55] M. F. Sanad, V. S. Chava, A. E. Shalan, L. G. Enriquez, T. Zheng, S. Pilla, S. T. Sreenivasan, *ACS Appl. Mater. Interfaces* **2021**, *13*, 40731.
[56] A. N. Nair, V. S. Chava, S. Bose, T. Zheng, S. Pilla, S. T. Sreenivasan, *ACS Sustainable Chem. Eng.* **2020**, *8*, 16565.
[57] X.-D. Wang, H.-Y. Chen, Y.-F. Xu, J.-F. Liao, B.-X. Chen, H.-S. Rao, D.-B. Kuang, C.-Y. Su, *J. Mater. Chem. A* **2017**, *5*, 7191.
[58] Y. Ma, X. Zhao, M. Niu, W. Li, X. Wang, C. Zhai, T. Wang, Y. Tang, X. Dai, *RSC Adv.* **2017**, *7*, 4124.
[59] S. Mu, M. Wang, H. Peelaers, C. G. Van de Walle, *APL Mater.* **2020**, *8*, 091105.
[60] K. Maeda, K. Teramura, T. Takata, M. Hara, N. Saito, K. Toda, Y. Inoue, H. Kobayashi, K. Domen, *J. Phys. Chem. B* **2005**, *109*, 20504.
[61] Z. Duan, G. Henkelman, *ACS Catal.* **2019**, *9*, 5567.
[62] C. Wei, Z. J. Xu, *Small Methods* **2018**, *2*, 1800168.
[63] J. M. Buriak, C. Toro, K.-S. Choi, *Chem. Mater.* **2018**, *30*, 7325.
[64] L. Yu, Z. Ren, *Mater. Today Phys.* **2020**, *14*, 100253.
[65] D. Voiry, M. Chhowalla, Y. Gogotsi, N. A. Kotov, Y. Li, R. M. Penner, R. E. Schaak, P. S. Weiss, *ACS Nano* **2018**, *12*, 9635.
[66] J. G. Chen, C. W. Jones, S. Linic, V. R. Stamenkovic, *ACS Catal.* **2017**, *7*, 6392.
[67] C. C. McCrory, S. Jung, J. C. Peters, T. F. Jaramillo, *J. Am. Chem. Soc.* **2013**, *135*, 16977.
[68] S. Jung, C. C. McCrory, I. M. Ferrer, J. C. Peters, T. F. Jaramillo, *J. Mater. Chem. A* **2016**, *4*, 3068.
[69] G. Kresse, J. Furthmüller, *Phys. Rev. B* **1996**, *54*, 11169.
[70] K. Momma, F. Izumi, *J. Appl. Crystallogr.* **2011**, *44*, 1272.